ORIGINAL PAPER

CrossMark

Effect of IL incorporation on ionic transport in PVdF-HFP-based polymer electrolyte nanocomposite doped with NiBTC-metal-organic framework

Rituraj Dutta[1] · A. Kumar[1]

Abstract

Ni-based metal-organic framework (MOF), nickel 1,3,5-benzene tricarboxylate (NiBTC) has been synthesized by solvothermal method and incorporated with ionic liquid (IL) 1-butyl-3-methylimidazolium tetrafluoroborate (BMIMBF$_4$) at varying weight ratios to use as nanofiller in the polymer matrix of poly (vinylidene fluoride-co-hexafluoropropylene) (PVdF-HFP). The structural properties of MOF-NiBTC-based composite polymer electrolyte system upon IL incorporation have been investigated by XRD, FTIR, BET, scanning EXAFS and XANES techniques. Shifting of vibrational modes of –COOH groups is observed from FTIR spectra due to strong interaction of Ni metal cluster with BF$_4^-$ anion of the IL. Local coordination structure and oscillation periodicity of Ni K-edge are investigated in R-space and k-space from the EXAFS as well as XANES spectra. Asymmetric oscillatory behavior with reduction in coordination number is observed upon IL incorporation due to strong interaction of guest IL with the host MOF-NiBTC. Dielectric relaxation and scaling of AC conductivity have been analyzed in the temperature range of 300–380 K and frequency range of 42 Hz–5 MHz. Non Debye type dielectric relaxation dynamics is observed due to short range hopping of ions. Ion concentration and temperature independent scaling behaviors are followed by the composite polymer electrolyte membranes. Optimum ionic conductivity of 6.5×10^{-3} S cm^{-1} and electrochemical stability up to 5.7 V have been obtained at 50 wt% of IL incorporation in the porous nanocomposite electrolyte system.

Keywords Metal-organic framework · Composite polymer electrolyte · Ionic liquid · Dielectric relaxation, AC conductivity

Introduction

Metal-organic frameworks (MOFs) are microporous hybrid nanomaterials composed of unsaturated inorganic metal clusters linked with organic linker molecules [1]. Due to their tremendous unique properties like high surface area, tunable topological geometry, controllable pore textures they are promising materials for various catalytic, sequestration, sensing and electrochromic applications [2]. MOFs can be treated as potential host materials for entrapping tiny guest molecules inside their micropores so that their phase behavior can be maintained by tunable guest-host interactions [3]. Ionic liquids (ILs) are highly stable room temperature molten salts composed of organic cations and inorganic anions with infinite structural variations. They have also special properties

such as high electrochemical and thermal stability, low vapor pressure and high ionic conductivity [4]. ILs can be used as highly preferable ionic guest materials to incorporate in the micropores of MOFs so that strong interaction of ions of IL and MOF can control the phase dynamics of the composite system via nanosizing effect of IL [5]. Confinement of IL in the micropores of different MOF materials to enhance structural as well as electrochemical properties has been reported by several researchers. Yifei Chen et al. [6] reported experimental as well as simulation work on confinement of IL 1-Butyl-3-methylimidazolium hexafluoro phosphate (BMIMPF$_6$) in IRMOF-1. The anionic part PF$_6^-$ exhibits strong interaction with the Zn metal cluster while the cationic part BMIM$^+$ resides at the open pores and reacts with the organic ligands. Kazuyuki Fujie et al. [7] reported the controlled phase dynamics of the framework ZIF-8 by incorporating IL EMI-TFSA in a view to enhance the electrochemical properties of the composite system. X-ray absorption near edge structure (XANES) and extended X-Ray absorption fine structure (EXAFS) are widely used techniques to elucidate the local structural geometry of the unsaturated inorganic metal

✉ A. Kumar
 ask@tezu.ernet.in

[1] Materials Research Laboratory, Department of Physics, Tezpur University, Napaam, Tezpur, Assam 784028, India

unit of MOFs and their tunable interactions with tiny guest molecules. XANES and EXAFS studies at Cu K-edge have been reported by C. Prestipino et al. [8] to investigate the local Cu^{2+} coordination of dehydrated HKUST-1. Xinxin Sang et al. [9] observed the comparative XANES and EXAFS at Zr K-edge to determine the crystallization rate of UiO-66 frameworks separately dissolved in ionic liquid and N-N-Dimethyl Formamide. Luisa Sciortino et al. [10] studied the local geometry and modeling of coordination numbers of FeBTC MOF by XANES and EXAFS and proposed that the locally ordered building blocks are in Fe^{+3} states. F. L. Morel et al. [11] studied the topological environment in phosphine and phosphine oxide functionalized MOF by P K-edge XANES. Maike Muller et al. [12] reported the XANES and EXAFS studies on MOF-5 upon incorporation of Cu and ZnO nanoparticles to use as catalyst for methanol synthesis. Solid polymer electrolytes are ionically conducting solvent free system and have several advantages over liquid electrolytes such as, no leakage, wide electrochemical stability, high compatibility etc. For the development of energy storage and conversion devices including Li ion batteries, intensive research works are going on solid polymer electrolytes. The ion conductive behavior of poly (ethylene oxide) (PEO) has been reported first by P.V. Wright in 1975 [13]. As the conventional polymer electrolytes exhibit low ionic conductivity ($\sim 10^{-5}$ to 10^{-7} S cm^{-1}) at room temperature, addition of ionic liquids to polymer networks results in better ionic conductivity as well as wide electrochemical stability. Anji Reddy Polu et al. [14] reported the room temperature ionic conductivity of 1.85×10^{-4} S cm^{-1} obtained by incorporation of ionic liquid EMIMTFSI into poly (ethylene oxide) (PEO)-based composite polymer electrolyte system. J. Pitawala et al. [15] reported the incorporation of pyrrolidinium-based ionic liquid into PVdF-HFP electrolyte system to obtain ionic conductivity of 1.6×10^{-3} S cm^{-1} at room temperature. A. Hofmann et al. [16] studied the effect of IL incorporation into polymer networks of PVdF-HFP and obtained optimum ionic conductivity of $\sim 2 \times 10^{-3}$ S cm^{-1} and electrochemical stability up to 5 V. It has been already reported that addition of nanosized filler materials can influence the electrochemical properties as well as compatibility of the polymer electrolyte system. The agglomeration rate of the polymer chain can be maintained by addition of nanofillers at specific concentration [17]. F. Croce et al. [18] synthesized the PEO-LiClO$_4$-based composite polymer electrolyte system and observed significant improvement in electrochemical properties upon incorporation of Al$_2$O$_3$ and TiO$_2$ ceramic fillers. W. Wieczorek et al. [19] reported the mechanism of Lewis base-acid interaction in PEO-NaI composite polymer electrolyte with incorporated nanofillers. MOFs can be treated as suitable nanofillers to be incorporated in polymer electrolyte matrix to improve their physicochemical properties. Studies on IL incorporated MOF nanocomposites have been reported by several researchers for different

electrochromic applications [6, 7]. Work on MOF-based polymer electrolyte membranes have also been reported for use in energy storage and conversion devices. Synthesis of highly compatible nanocomposite polymer electrolyte incorporated with Al-based MOF has been reported by Claudio Gerbaldi et al. [20] with excellent improvement in cyclic profile. Synthesis of polymer electrolyte membranes using IL incorporated MOF nanocomposites as filler materials have not been reported yet. Addition of IL can generate more free space in the micropores of MOF for cationic transport as the anionic part of IL is closely packed or confined towards the metal cluster. The cations mostly reside at the open pores and can hop from one coordination site to another in the polymer matrix to enhance the electrochemical performances Scheme 1.

In this present work, NiBTC-MOFs have been synthesized and incorporated with different wt% of IL 1-butyl-3methylimidazolium tetrafluoroborate by solvothermal process. The effect of IL incorporation in MOF-NiBTC nanocomposites dispersed in the polymer poly (vinylidene fluoride-co-hexafluoropropylene) (PVdF-HFP) matrix has been investigated. Their structural properties have been investigated by scanning XANES and EXAFS to gain an insight into the local geometry and coordination of IL ions in MOF framework. Dielectric relaxation dynamics, electrochemical stability, variation of AC conductivity and scaling behavior have also been studied in the present work.

Experimental

Materials

All the chemicals used in the present work were used as-received without further purification. Nickel (II) nitrate hexahydrate (Ni(NO$_3$)$_2$·6H$_2$O) (purity: $\geq 98.0\%$, molecular weight: 290.81 g/mol), N-N-dimethyl formamide (DMF) (purity: $\geq 99.0\%$, molecular weight: 73.09 g/mol), 1,3,5-benzenetricarboxylic acid (H$_3$BTC) (purity: $\geq 98.0\%$, molecular weight: 210.14 g/mol), triethylamine (purity: $\geq 99.0\%$, molecular weight: 101.19 g/mol), methanol (purity: $\geq 99.0\%$, molecular weight: 32.048 g/mol), ethanol (purity: $\geq 99.9\%$, molecular weight: 46.078 g/mol) and acetonitrile (purity: $\geq 99.0\%$, molecular weight: 41.05 g/mol) were purchased from Merck. Poly (vinylidene fluoride-co-hexafluoropropylene) (PVdF-HFP) (purity: $\geq 99.0\%$, molecular weight: 400000 g/mol) and 1-butyl-3-methylimidazolium tetrafluoroborate (BMIMBF$_4$) (purity: $\geq 98.0\%$, molecular weight: 226.02 g/mol) were procured from Sigma Aldrich.

Synthesis of MOF-NiBTC

MOF-NiBTC has been prepared by solvothermal synthesis method. 10 mmol of both Ni (NO$_3$)$_2$·6H$_2$O and H$_3$BTC were
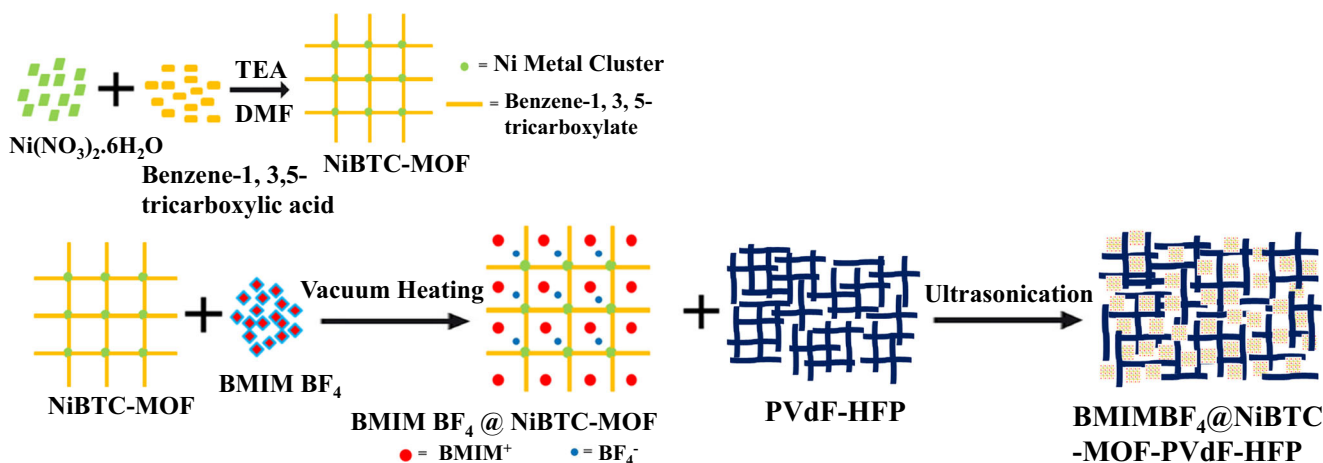
Scheme 1 Schematic representation for synthesis of IL incorporated NiBTC-MOF-based PVdF-HFP nanocomposite

dissolved separately in 30 ml DMF. The two solutions were mixed together and stirred for 24 h at room temperature [21]. A precipitate was obtained by centrifugation and the liquid portion was decanted. The precipitate was washed thrice with DMF and Methanol to remove the unreacted Ni $(NO_3)_2.6H_2O$. The precipitate was heated at 373 K under vacuum for 12 h to remove the DMF from the tiny micropores [22, 23] and pale green colored product was obtained.

Incorporation of IL in MOF-NiBTC

1-Butyl-3-methylimidazolium tetrafluoroborate (BMIMBF$_4$) has been incorporated into the micropores of MOF-NiBTC at 30, 40 and 50 wt% of IL and MOF. The IL-MOF nanocomposites were prepared by mixing with pestle and mortar and heating at 373 K for 12 h to dry off the water content and for homogeneous distribution of IL in the pores of MOF.

Preparation of IL incorporated MOF-NiBTC-based PVdF-HFP nanocomposite membranes

To prepare the polymer matrix, 1 g of pre-dried PVdF-HFP was dissolved in 20 ml of acetonitrile and ultrasonicate for 2 h. IL has been incorporated in MOF by mixing and vacuum heating at 373 K for 12 h to dry off the water content. Only after vacuum drying, the IL@MOF composites are dispersed in PVdF-HFP matrix. For that 0.5 g of pristine MOF-NiBTC and each of 30, 40 and 50 wt% IL incorporated MOF-NiBTC nanocomposites were dispersed separately in the PVdF-HFP matrix by ultrasonication. Each of the IL incorporated MOF-NiBTC-based PVdF-HFP composite electrolyte solutions was cast onto glass slides. After room temperature drying for 2 h greenish white colored flexible self-standing membranes were obtained that were taken for further characterizations.

Characterization techniques

XRD patterns of pristine and IL incorporated MOF-NiBTC-based PVdF-HFP nanocomposites were obtained by Bruker AXS D8 X-ray Diffractometer in the 2θ range of 5° to 90°. The FTIR spectra were recorded by Nicolet Impact 410 spectrometer in the range of 400 to 4500 cm^{-1}. The scanning X-ray absorption near edge structure (XANES) and extended X-ray absorption fine structure (EXAFS) data were obtained by synchrotron beamline in transmission mode having 2.5 GeV bending magnet source with flux of 10^{11} photon/s in the energy range of 4.25 keV. The incident photon energy resolution ($E/\Delta E$) was 10^4 with beam size ($H \times V$) of 1 mm × 0.2 mm. The N$_2$ adsorption desorption isotherms of the nanocomposites were obtained by using BET Surface area analyzer (NOVA 1000 E). The size, shape and distribution of the nanoparticles have been observed by transmission electron microscope (TECNAI G2 20 S-TWIN). Dielectric and AC impedance measurements were investigated by Hioki 3532-50 LCR Hitester in the frequency range of 42 Hz to 5 MHz and in the temperature range of 300 to 380 K. The electrochemical stability analysis was done by Linear Sweep Voltammetry using Autolab (PGSTAT 302 N).

Results and discussion

X-ray diffraction analysis

The XRD patterns of PVdF-HFP, IL BMIMBF$_4$ and NiBTC-MOF are presented in Fig. 1(a). The characteristic peaks at $2\theta = 8°$ corresponds to the (110) planes and $2\theta = 12$ ° corresponds to the (300) planes of NiBTC-MOF and the (010) planes of IL BMIMBF$_4$. The peak at $2\theta = 19.7°$ corresponds to the (020) planes of PVdF-HFP. The XRD patterns of
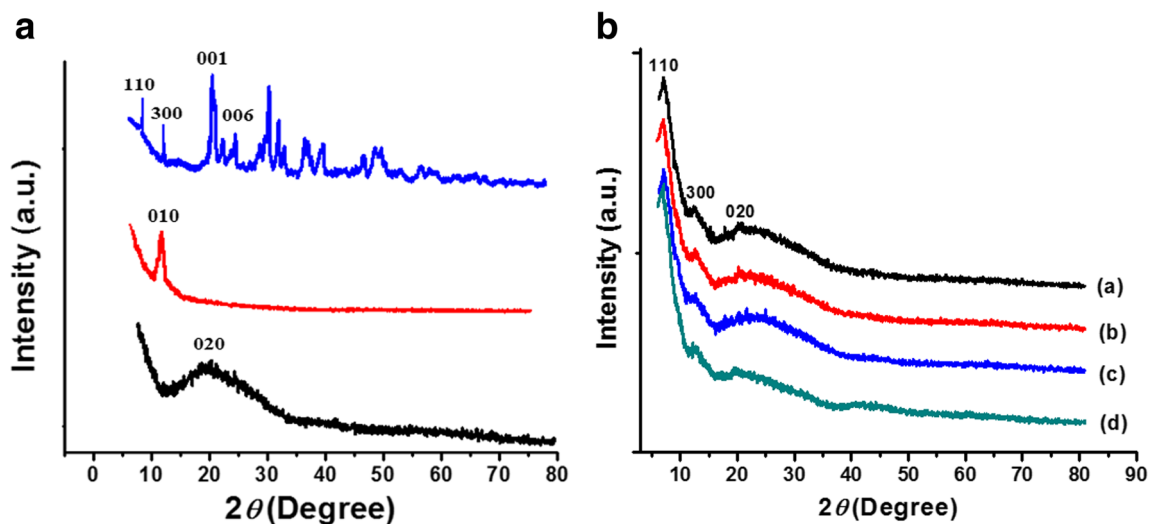
Fig. 1 **a** X-ray diffraction patterns of (a) PVdF-HFP, (b) BMIMBF$_4$, (c) NiBTC-MOF. **b** X-ray diffraction patterns of pristine and IL incorporated MOF-NiBTC-based PVdF-HFP nanocomposites where, (a) 0 wt% IL, (b) 30 wt% IL, (c) 40 wt% IL, (d) 50 wt% IL

pristine MOF-NiBTC and IL incorporated MOF-NiBTC based PVdF-HFP nanocomposites are presented in Fig. 1(b). Incorporation of IL with increasing wt% increases the amorphicity of the nanocomposites owing to the interaction of BMIM$^+$ cations of IL with the linker molecules of MOF-NiBTC and the BF$_4^-$ anions of IL with the Ni metal cluster of MOF. The cationic part of IL i.e. BMIM$^+$ can also interact with the fluorine atoms of the PVdF-HFP chain, that contribute to reduce the crystallinity of the nanocomposites [24]. The % degree of crystallinity (X_c) for pristine MOF-NiBTC and different wt% of IL incorporated MOF-NiBTC-PVdF-HFP nanocomposites has been obtained according to Eq. (1) and the values are depicted in Table 1.

$$X_c = \left(\frac{A}{A_T}\right)\cdot 100\% \tag{1}$$

where A_T is the total area under the domain of the whole diffractogram and A is the area under the particular crystalline diffraction peak. For better understanding of the XRD patterns, crystallite sizes of the nanocomposites have been determined by measuring the FWHM of the PVdF-HFP peak and are depicted in Table 1. The crystallite size of the nanocomposites is found to decrease upon incorporation of IL because of enhancement in amorphicity with increasing IL loading.

Table 1 The % degree of crystallinity and crystallite size of MOF-NiBTC-based composite polymer electrolyte at different wt% of IL

Wt% of IL	Degree of crystallinity (%)	Crystallite size (Å)
0%	23.7	0.428
30%	21.4	0.397
40%	17.9	0.316
50%	13.8	0.290

The Scherrer formalism was used to determine the crystallite size $(L) = \frac{K\lambda}{\beta cos\theta}$ for a crystalline peak with FWHM β measured at diffraction angle 2θ. K (~ 0.89) denotes the Scherrer constant of proportionality and λ is the wavelength of the Cu K$_\alpha$ (1.5406 Å) X-ray used.

FTIR analysis

FTIR spectra of MOF-NiBTC-based PVdF-HFP nanocomposites with different wt% of IL have been presented in Fig. 2. Interaction of ions of IL with MOF-NiBTC and also with PVdF-HFP can affect the characteristic vibrational modes as the interaction between the metal cluster and the linker molecules of MOF becomes weaker upon incorporation
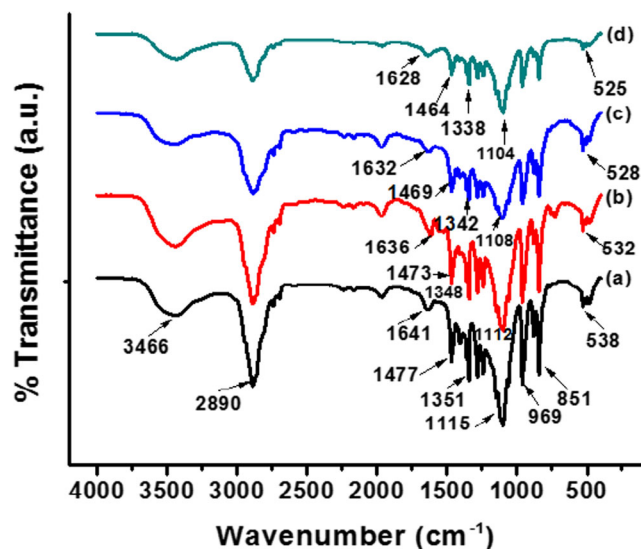

Fig. 2 FTIR spectra of pristine and IL incorporated MOF-NiBTC-based PVdF-HFP nanocomposites where, (a) 0 wt% IL, (b) 30 wt% IL, (c) 40 wt% IL, (d) 50 wt% IL

of IL. In the pristine MOF-NiBTC-based PVdF-HFP nanocomposites, characteristic peaks appear at 1115 cm^{-1} and 1351 cm^{-1} due to the symmetric stretching vibration of –COOH group present in the linker molecules of MOF-NiBTC [25]. At 1477 cm^{-1} and 1671 cm^{-1}, peaks appear because of the asymmetric stretching and bending vibrations of –COOH group, respectively. Upon IL incorporation, the peaks of –COOH vibrational bonds shift towards lower wave number positions. The peak at 1115 cm^{-1} shifts to 1104 cm^{-1}, 1351 cm^{-1} shifts to 1338 cm^{-1}, 1477 cm^{-1} shifts to 1464 cm^{-1} and the peak 1641 cm^{-1} shifts to 1628 cm^{-1} in the 50 wt% IL incorporated MOF-NiBTC-PVdF-HFP nanocomposites. Also the stretching vibrational mode of Ni-O shifts from 538 cm^{-1} and 525 cm^{-1} towards lower wave number positions upon incorporation of IL. The shifting of modes towards lower wave number positions can be attributed to the elongation of the chemical bonding between the MOF metal cluster and the linker molecules due to interaction of ions of IL. At 3466 cm^{-1} a broad peak appears due to the hydroxyl (–OH) group present both in MOF-NiBTC and IL BMIMBF$_4$ [26]. At 2890 cm^{-1} one significant peak is observed for –C–H stretching vibration in PVdF-HFP chain [27, 28]. Other peaks at 969 cm^{-1} and 851 cm^{-1} are respectively due to –OH bending vibration of aromatic compound and –C–H out of plane bending vibration present in MOF-NiBTC [29, 30].

Scanning EXAFS and XANES analysis

EXAFS and XANES techniques have wide impact on analyzing the local coordination structures of unsaturated inorganic metal nodes in MOF materials. Scanning EXAFS and XANES spectra of pristine and IL incorporated MOF-NiBTC nanocomposites have been observed to determine the absorption characteristics and phase behavior dynamics of the metal (Ni) K-edge upon IL incorporation. The absorption coefficient in transmission mode can be expressed as, $I = I_0 \exp.[-\mu(E)x]$, where I_0 is the photon beam being incident on material, I is the photon beam transmitted from the surface of the material having absorption coefficient $\mu(E)$ and x is the distance travelled by the beam. The XANES spectra have been recorded in the energy from 8300 to 8475 eV and the EXAFS spectra from 8150 to 9050 eV. From the EXAFS spectra shown in Fig. 3(a) Ni K-edge peak of MOF-NiBTC observed at 8350 eV can be compared to Ni-Ni first shell peak of pure Ni foil used as reference material. This confirms that the Ni species has the oxidation state of +2. The absorption coefficients of Ni K-edges are observed to increase from 0.86 to 5.01 with increasing wt% of IL. After Ni K-edge the first resonance peak is clearly observed in XANES spectra around 8394 eV shown in Fig. 3(b) and can be attributed to Ni-O bonding. At around 8333 eV, a weak shoulder pre-edge peak appears that can be ascribed to 1 s → 3d quadrapolar transition. An increase in small pre-edge peak is observed around

8333 eV upon IL incorporation as confinement of IL can destroy the original crystal structure of pristine MOF. The XANES spectra at k-space (Fig. 3(c)) and EXAFS spectra at R-space (Fig. 3(d)) have been derived from Athena software to understand the periodic oscillation and coordination of Ni metal node with IL loading. For IL incorporated samples certain mismatch or heterogeneity has been observed in oscillation periodicity from $k = 9$ Å^{-1}. This can be attributed to the deformation of first shell Ni-O bonding as strong interaction of Ni metal nodes with BF$_4^-$ anion can weaken the metal–ligand interaction of MOF. Dehydration of the metal cluster may induce certain changes in the coordination of the Ni first shell. In R-space, at 0.65 Å and 1.59 Å two distinct peaks corresponding to oxygen and nickel are observed to be reduced to 0.61 Å and 1.54 Å after IL incorporation. It suggests the reduction of coordination number as a result of first shell dehydration of nickel metal cluster with increasing incorporation of IL [9, 10].

N$_2$ adsorption-desorption analysis

N$_2$ adsorption-desorption isotherms of pristine and IL incorporated MOF-NiBTC-based PVdF-HFP nanocomposites have been recorded at liquid N$_2$ temperature (77 K) to observe the changes in pore parameters upon IL incorporation and depicted in Fig. 4. Agglomeration of MOF nanoparticles may form granular morphology within the polymer matrix due to the formation of mesopores as observed from TEM results. The N$_2$ adsorption-desorption isotherms reveal hysteresis behavior at high relative pressure owing to the presence of mesopores in the nanocomposite system [7]. With increasing wt% of IL, N$_2$ adsorption decreases at low relative pressure as IL is mostly confined at micropores of MOF-NiBTC rather than at mesopores. As some portions of pristine MOF-NiBTC structure may get collapse upon IL incorporation, total surface area and total pore volume of the nanocomposites are observed to be decreased with increasing wt% of IL and depicted in Table 2.

Morphological analysis

Figure 5 [(a)-(d)] depicts the transmission electron microscope (TEM) micrographs of pristine and IL incorporated MOF-NiBTC-based PVdF-HFP nanocomposites having average particle size of 2 nm at different wt% of IL. Upon IL incorporation, the distribution of MOF nanoparticles within the polymer matrix is observed to be more uniform due to the confinement effect of IL in the micropores of MOF. Electrostatic interaction of the BF$_4^-$ anion with the Ni metal cluster and BMIM$^+$ cation with the organic linkers of MOF as confirmed from the FTIR results can reduce the free space leading to compact and ordered structure of nanoparticles in the porous polymer matrix. Appearance of agglomerated granular
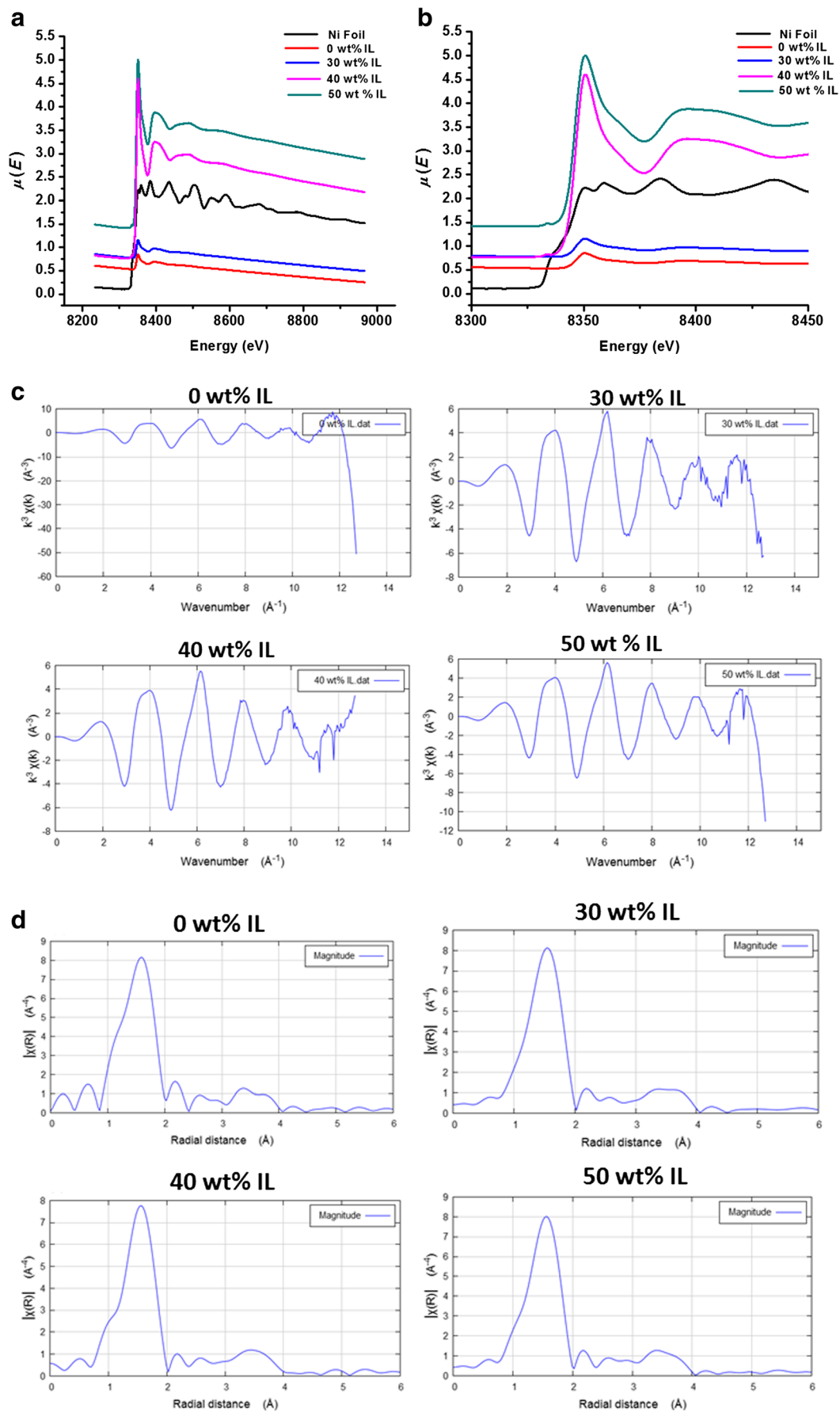
Fig. 3 **a** Scanning EXAFS spectra of MOF-NiBTC-based PVdF-HFP nanocomposites at different wt% of IL. **b** Scanning XANES spectra of MOF-NiBTC-based PVdF-HFP nanocomposites at different wt% of IL. **c** Scanning XANES spectra at *k*-space for MOF-NiBTC-based PVdF-HFP nanocomposites at different wt% of IL. **d** Scanning EXAFS spectra at R-space for MOF-NiBTC-based PVdF-HFP nanocomposites at different wt% of IL

morphology of the nanocomposites can be attributed to the formation of mesopores [7]. The TEM micrograph for NiBTC-MOF in Fig. 5(e) exhibits granular agglomerated morphology with average particle size of 2 nm.

Analysis of dielectric permittivity

The dielectric permittivity of a disordered material can be expressed as,

$$\varepsilon^*(\omega) = \frac{1}{i\omega C_0 Z^*(\omega)} = \varepsilon'(\omega) - i\varepsilon''(\omega) \qquad (2)$$

Where the real part reveals dielectric permittivity and the imaginary part implies dielectric energy loss in every cycle. C_0 is the free space capacitance that can be denoted as $C_0 = \frac{\varepsilon_0 A}{d}$ [31]. The dielectric permittivity ε' and dielectric loss ε'' can be denoted in context of real (Z') and imaginary (Z') parts of impedance as follows:

$$\varepsilon'(\omega) = -\frac{1}{C_0\omega}\left[\frac{Z'}{Z'^2 + Z'^2}\right] \qquad (3)$$

$$\varepsilon''(\omega) = \frac{1}{C_0\omega}\left[\frac{Z'}{Z'^2 + Z'^2}\right] \qquad (4)$$

The dielectric relaxation dynamics have been analyzed using Havriliak Nigami (HN) approximation as,
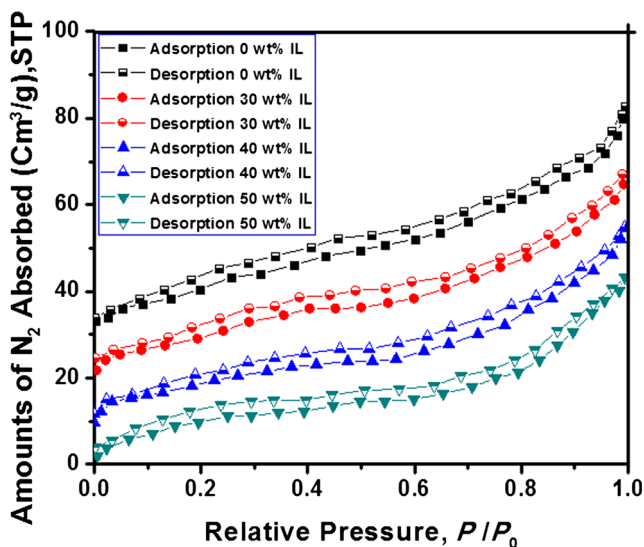

Fig. 4 N$_2$ adsorption-desorption isotherms of MOF-NiBTC-based PVdF-HFP nanocomposites at different wt% of IL

Table 2 BET surface area and pore volume of MOF-NiBTC-based composite polymer electrolyte at different wt% of IL

Wt% of IL	Total surface area (S_{BET}) (m^2/g)	Pore volume (cm^3/g)
0%	1154	0.62
30%	957	0.53
40%	845	0.44
50%	578	0.35

$$\varepsilon^*(\omega) = \varepsilon_\infty + \frac{\Delta\varepsilon}{\left[1 + (i\omega\tau)^{\beta_{HN}}\right]^{\alpha_{HN}}}, \quad 0 \le \beta_{HN}\alpha_{HN} \le 1 \qquad (5)$$

where $\Delta\varepsilon = \varepsilon_s - \varepsilon_\infty$, ε_∞ and ε_s are dielectric permittivity at high and low frequencies respectively. β_{HN} and α_{HN} are parameters that reveal symmetric and asymmetric distribution respectively for the relaxation dynamics where as $\alpha_{HN} = 1$ for Cole-Cole model , $\beta_{HN}=1$.

for Davison-Cole model and $\beta_{HN} =\alpha_{HN} = 1$ for Debye model [32].

From the Eq. (6) ε' can be formulated as

$$\varepsilon^*(\omega) = \varepsilon_\infty + \text{Re} \frac{\Delta\varepsilon}{\left[1 + (i\omega\tau)^{\beta_{HN}}\right]^{\alpha_{HN}}} \qquad (6)$$

Figure 6(a) shows the plots for real part of permittivity vs. angular frequency ω of the nanocomposites system at different wt% of IL. At low frequency, high value of dielectric constant exists as the electric dipoles can easily respond to the electric field because of interfacial polarization effect. As the ion concentration increases with increasing wt% of IL, accumulation of space charge at the electrode-electrolyte interfaces occurs due to dipolar mismatch as well as localized charge carriers available in charge defect centers that in turn enhance dielectric permittivity. At high frequency region, electric dipoles are unable to respond to the quickly changing electric field and dielectric permittivity decreases [33]. The permittivity data have been fitted according to Eq. (6) and different fitting parameters have been presented in Table 3.

Figure 6 (b) represents the plots for dielectric loss ε'' vs. angular frequency for pristine and IL incorporated MOF-NiBTC-based PVdF-HFP nanocomposites at room temperature. Dielectric loss is affected by the contribution from Maxwell-Wagner interfacial polarization (ε''_{MW}), dc conductance (ε''_{dc}), and Debye loss factor (ε''_{D}). It is observed that dielectric loss decreases with increasing frequency and no well-defined relaxation peak is formed because of less contribution from interfacial polarization effect [34]. As the cationic part BMIM$^+$ can interact with nearby polymer segments so increase in ion mobility also influences dielectric loss with increasing wt% of IL.

Fig. 5 Transmission electron microscopy (TEM) micrographs of pristine and IL incorporated MOF-NiBTC-based PVdF-HFP nanocomposites where (a) 0 wt% IL, (b) 30 wt% IL, (c) 40 wt% IL and (d) 50 wt% IL, (e) NiBTC-MOF
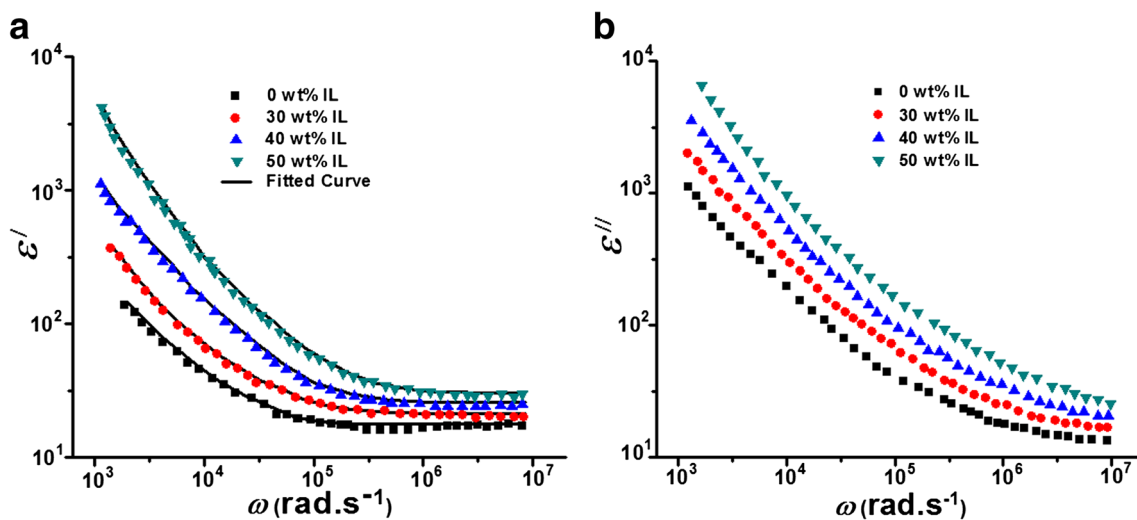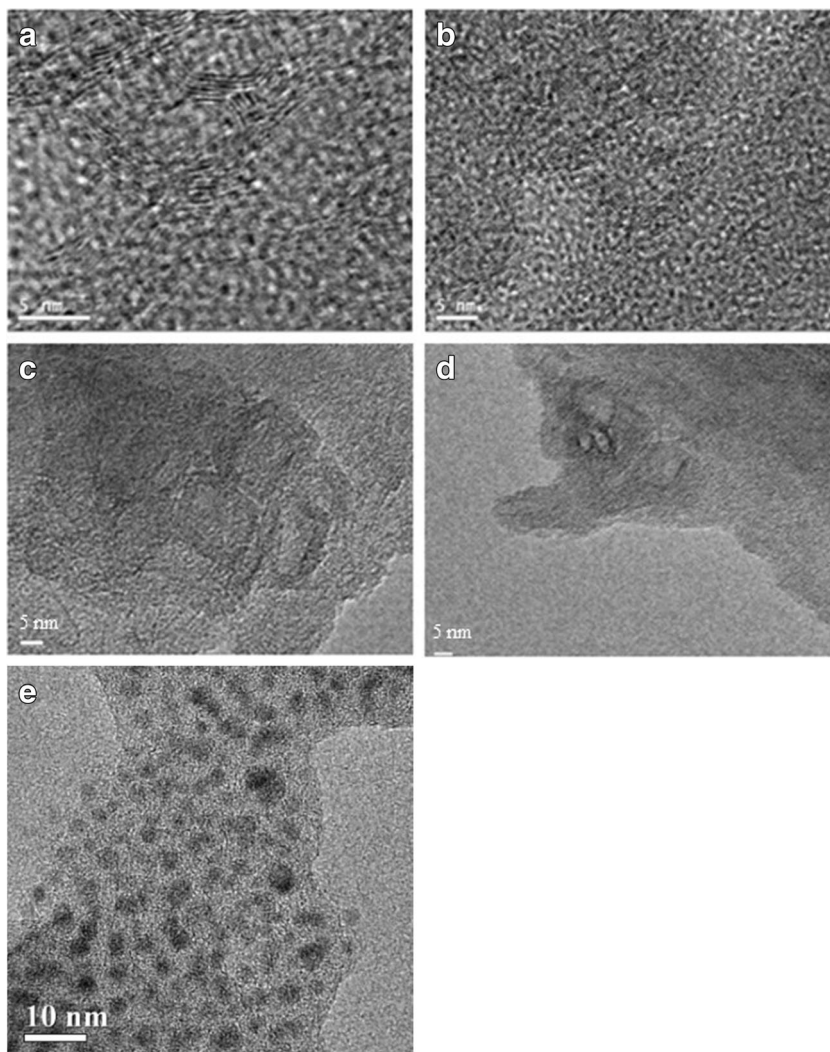

Fig. 6 **a** Real part of permittivity vs. angular frequency plots for MOF-NiBTC-based PVdF-HFP nanocomposites at different wt% of IL at room temperature (300 K). **b** Imaginary part of permittivity vs. angular frequency plots for MOF-NiBTC-based PVdF-HFP nanocomposites at different wt% of IL at room temperature (300 K)

Table 3 HN parameters for room temperature variation of ε' with angular frequency for MOF-NiBTC-based composite polymer electrolyte at different wt% of IL

Wt% of IL	ε_∞	$\Delta\varepsilon$	β_{HN}	α_{HN}
0%	25	136	0.62	0.92
30%	33	576	0.59	0.94
40%	42	945	0.55	0.96
50%	51	1789	0.51	0.98

Dielectric modulus analysis

The dielectric modulus formalism can be represented as reciprocal of dielectric permittivity and can be denoted as,

$$M^*(\omega) = M'(\omega) + i\,M''(\omega) \tag{7}$$

where $M'(\omega) = \frac{\varepsilon'(\omega)}{\varepsilon'^2(\omega)+\varepsilon''^2(\omega)}$ and $M''(\omega) = \frac{\varepsilon''(\omega)}{\varepsilon'^2(\omega)+\varepsilon'^2(\omega)}$

Figure 7(a) and (b) depicts the plots for real and imaginary parts of dielectric modulus vs. angular frequency for MOF-NiBTC based PVdF-HFP nanocomposites at different wt% of IL. M' increases with increasing angular frequency but no well-defined relaxation peaks are observed at higher frequency region. Due to negligible contribution of electrode polarization M' attains zero at low frequency region.

In M'' spectra certain dielectric loss peaks are observed corresponding to particular relaxation frequencies. The relaxation frequency (ω_{max}) is reciprocal to the relaxation time (τ) and so relaxation time decreases as the peaks are getting shifted towards higher frequency with increasing wt% of IL. At the point of relaxation frequency there occur transition from dc to ac conduction and ions follow frequency independent behavior.

The dielectric modulus M'' spectra can be fitted with Kohlrausch-Williams-Watts (KWW) approximation as follows:

$$M''(\omega) = \frac{M''_{max}(\omega)}{\left[(1-\beta_{KWW}) + (\beta_{KWW}/(1+\beta_{KWW}))\left\{\beta_{KWW}\left(\frac{\omega_{max}}{\omega}\right) + \left(\frac{\omega}{\omega_{max}}\right)^{\beta_{KWW}}\right\}\right]} \tag{8}$$

Where β_{KWW} is the non linear relaxation fitting parameter and its value lies between 0 and 1 [35]. KWW empirical model deals with asymmetric non Debye relaxation dynamics of short relaxation time and the values of β_{KWW} are observed to be decreased with increasing wt% of IL. The values of $M''_{max}(\omega)$, β_{KWW} and ω_{max} have been evaluated from the fitting curves and depicted in Table 4.

The temperature-dependent plots of imaginary part of modulus M'' vs. angular frequency for MOF-NiBTC-based PVdF-HFP nanocomposites at 50 wt% of IL have been presented in Fig. 7(c). It has been observed that the modulus peaks are
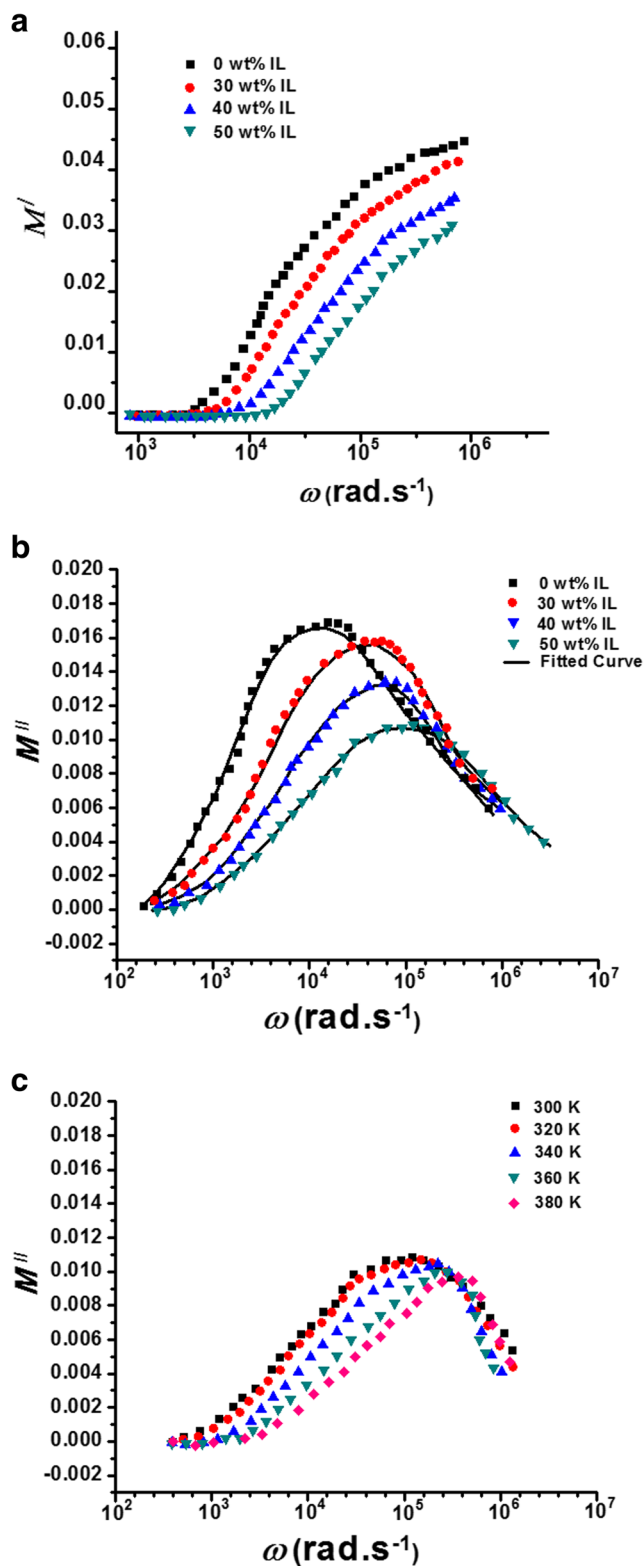
Fig. 7 **a** Real part of modulus vs. angular frequency plots for MOF-NiBTC-based PVdF-HFP nanocomposites at different wt% of IL at room temperature (300 K). **b** Imaginary part of modulus vs. angular frequency plots for MOF-NiBTC-based PVdF-HFP nanocomposites at different wt% of IL at room temperature (300 K). **c** Imaginary part of modulus vs. angular frequency plots for 50 wt% IL incorporated MOF-NiBTC-based PVdF-HFP nanocomposites at different temperatures

Table 4 M''_{max}, $\log\omega_{max}$, relaxation time (τ), and β_{KWW} for MOF-NiBTC-based composite polymer electrolyte at different wt% of IL (300 K)

Wt% of IL	M''_{max}	$\log\omega_{max}$	Relaxation time (τ)	β_{KWW}
0%	0.0169	7.659	2.19×10^{-8}	0.78
30%	0.0159	7.745	1.79×10^{-8}	0.76
40%	0.0148	7.772	1.68×10^{-8}	0.73
50%	0.0109	7.793	1.60×10^{-8}	0.70

getting shifted towards higher frequency region with increasing temperature and relaxation time decreases accordingly. This can be attributed to increase in mobility of ions in the vicinity of the polymer segments with increasing temperature [36]. At different relaxation frequencies the values of corresponding relaxation time are tabulated in Table 5.
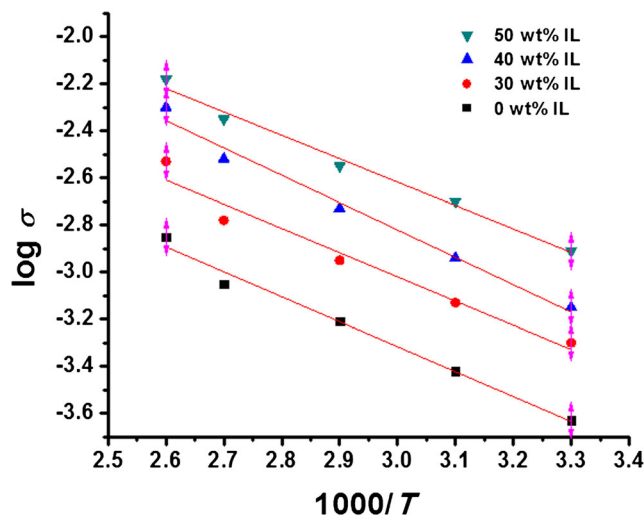
Ionic conductivity studies

The ionic conductivity of MOF-NiBTC based polymer electrolyte nanocomposites has been observed at room temperature and attained 1.5×10^{-3} S cm^{-1} at 50 wt% of IL. It has been reported that the viscosity of the imidazolium-based ILs decreases with increasing temperature that in turn intensify ionic conductivity. At varying temperature range from 300 K to 380 K ionic conductivity (σ) for MOF-NiBTC-based PVdF-HFP nanocomposite at different wt% of IL has been observed and presented in Fig. 8. With increasing temperature ionic conductivity increases due to enhanced mobility of ions along the segmental motion of polymer chain and attains 6.5×10^{-3} S cm^{-1} at 380 K. As temperature increases, expansion of polymer chain can generate more free channels for easy migration of charge carriers leading to enhance ionic conductivity [37]. According to Arrhenius formalism, ionic conductivity follows linear process that is related to activation energy (E_a) follows,

$$\sigma = \sigma_o \exp\left(\frac{-E_a}{K_B T}\right) \tag{9}$$

Table 5 $\log\omega_{max}$ and relaxation time (τ) for 50 wt% IL incorporated MOF-NiBTC-based composite polymer electrolyte at different temperatures

Temperature (K)	$\log\omega_{max}$ (rad s^{-1})	Relaxation time (τ)
300	7.793	1.60×10^{-8}
320	7.806	1.56×10^{-8}
340	7.828	1.48×10^{-8}
360	7.843	1.43×10^{-8}
380	7.855	1.39×10^{-8}

Fig. 8 Temperature-dependent ionic conductivity plots of IL incorporated MOF-NiBTC-based PVdF-HFP nanocomposites at different wt% of IL

The binding energy (E_b) and strain energy (E_s) can contribute to the activation energy of the charge carriers as,

$$E_a = E_b + E_s \tag{10}$$

Any ion has its binding energy (E_b) that is needed to leave its original site and strain energy (E_s) is required to create hopping channels for migration of ion to any neighboring coordination site. Increasing ion concentration can influence to expand the polymer segments that reduce the strain energy (E_s) [38]. According to Anderson-Stuart model, the binding energy E_b and strain energy (E_s) for any ion conducting material can be expressed as,

$$Eb = \frac{\beta z z_O e^2}{\gamma(r + r_O)} \tag{11}$$

$$Es = 4\pi . G r_d (r - r_d)^2 \tag{12}$$

Where β is the 'Madelung constant' that depends on the distance between neighboring ion sites, z and r are the charge state and radius of the cation, z_O and r_O are the charge state and radius of non-bridging oxygen ion, e is the charge of electron and γ is the covalency parameter that determines the rate of charge neutralization of the ion with its nearest neighbors, G is the elastic or shear modulus, r is the cation radius, r_d is the effective radius of the doorway for easy migration of the cation through the polymer segments. Hence, the activation energy E_a can be expressed in terms of E_b and E_s as,

$$Ea = \frac{\beta z z_O e^2}{\gamma(r + r_O)} + 4\pi . G r_d (r - r_d)^2 \tag{13}$$

From the slope of the plot of σ vs. 1000/T the activation energies of the composite polymer electrolyte at different wt%

of IL have been calculated and depicted in Table 6. With increasing wt% of IL the amorphicity of the composite polymer electrolyte enhances that can minimize the potential hopping barrier leading to reduce activation energy. The regression line (intercept) values are obtained from the linear fitted data and presented in Table 6. Dielectric relaxation studies show that the ion transport in MOF-NiBTC based PVdF-HFP nanocomposites is enhanced with increasing wt% of IL. This can be attributed to the plasticization effect of IL that increases the amorphicity of the composite system which is also confirmed from XRD results. The decrease in degree of crystallinity in turn reduces the energy barrier to intensify the segmental motion of PVdF-HFP chain [14]. Ion concentration as well as mobility of charge carriers contributes to the ionic conductivity of the composite electrolyte system. The transport mechanism for the nanocomposite electrolyte is both intrachain and interchain hopping. Addition of IL can generate more free space in the micropores of MOF for cationic transport as the anionic part of IL is closely packed or confined to the metal clusters. The cations mostly reside in the open pores and hop from one coordination site to another in the same polymer segment. The mobile cations can also interact with the anions of the polymer chain. As the polymer chains are interconnected, the cations can also migrate to the nearby polymer segments through the free volume channels and the mobility of ions is influenced by IL incorporation as well as increasing temperature [39–41].

AC conductivity variation with frequency

Figure 9 (a) depicts the AC conductivity variation at room temperature with frequency for MOF-NiBTC-based PVdF-HFP nanocomposites at different wt% of IL. Wide frequency range of 42 Hz–5 MHz has been employed for the dielectric relaxation as well as AC conductivity measurements for better convenience in data acquisition [33, 35, 36]. The AC conductivity plots exhibit plateau region at low frequency side that corresponds to DC conduction and spike region at high frequency side due to AC conduction [42]. The transmission of ions from DC to AC conduction can be explained by the power law equation:

Table 6 Activation energy (E_a) and regression line (intercept) value of MOF-NiBTC-based PVdF-HFP nanocomposites at different wt% of IL

Wt% of IL	Activation energy (E_a) (eV)	Regression line (intercept) value
0%	0.31	− 0.135
30%	0.29	0.063
40%	0.26	0.186
50%	0.23	0.345

$$\sigma = \sigma_0[1 + (f/f_0)^n] \qquad (14)$$

where σ_0 is the DC conductivity, f_0 is the characteristic hopping frequency and n is the frequency exponent [43]. The DC plateau region provides the evidence for the formation of ion conducting path throughout the polymer matrix. The DC conductivity arises from the long range motion of charges and the plateau region due to DC conductivity extrapolates to zero frequency. With increasing frequency, both DC and AC conductivity contribute to the overall conductivity that increases with frequency. At lower frequencies, charge carriers pass through long pathways and is dominated by bottlenecks of low conducting regions and at higher frequencies, localized charge motion contributes to the AC conductivity. According to jump relaxation model, the hopping of charge carriers occur from one coordination site to the adjacent ones after crossing over activated diffusion barriers. Translational hopping of charge carriers occurs at lower frequencies while at higher frequencies conductivity is dominated by localized orientational hopping. Before completing any successful hopping ions have to undergo several forward and backward hops and the type of hopping whether it is forward or backward can be determined by the frequency exponent n. Low values of frequency exponent depict short range forward hopping whereas high values of frequency exponent reveal long range backward hopping of mobile ions [44]. The range of frequency exponent 'n' is $0 < n < 1$ for short range forward hopping and greater than or equal to unity for long range backward hopping. Based on the concept of jump relaxation model, the frequency dependence of AC conductivity can be interpreted by mismatch and relaxation of charge carriers. According to this approximation, any mobile charge carrier can experience an effective potential at a position r by the superposition of two different potentials: cage effect or columbic potential $V_c(r)$ and periodic lattice potential $V_p(r)$. The effective potential $V(r)$ can be denoted as the sum of $V_c(r)$ and $V_p(r)$. When an ion hops from one coordination site to any neighboring site, mismatch is generated as the nearby sites are already occupied by neighboring ions. The mismatch can be minimized by two effective ways: (i) the mobile ion returns to its previous position keeping the effective potential unchanged. The AC conductivity is not affected by this type of correlated hopping process. (ii) The neighboring atoms in the new sites get rearranged and the cage effect potential changes by the columbic interactions leading to minimize the effective potential, $V(r)$. The mobile ion experiences energetically favorable effective potential to complete hopping successfully and in turn contribute to enhance the AC conductivity. The plots of
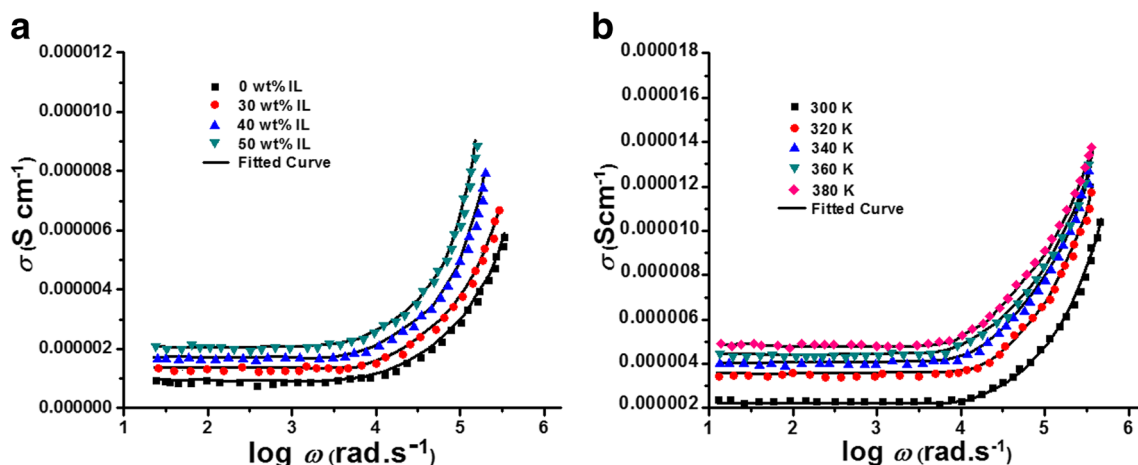
Fig. 9 **a** AC conductivity vs. angular frequency plots for MOF-NiBTC-based PVdF-HFP nanocomposites at different wt% of IL at room temperature (300 K). **b** Temperature-dependent AC conductivity vs. angular frequency plots for MOF-NiBTC-based PVdF-HFP nanocomposites at 50 wt% of IL

AC conductivity vs. angular frequency have been fitted with the Eq. (14) and the values of frequency exponent are observed to be decreased with increasing wt% of IL and presented in Table 7.

The variation of AC conductivity with angular frequency have been observed for 50 wt% of IL in the temperature range 300 to 380 K and the curves are fitted according to Eq. (14) and presented in Fig. 9 (b). As temperature increases mobility of the ions as well as segmental motion of polymer chain increases leading to short range hopping of ions in DC to AC transition regions. With increasing temperature lower values of frequency exponent are obtained from the fitted curves due to frequent forward hopping and are depicted in Table 8.

Scaling of AC conductivity with frequency

The characteristic frequency of AC conduction can be considered as:

$$f_0 = \sigma_0 / \varepsilon_0 \Delta\varepsilon, \tag{15}$$

The scaling condition of AC conductivity with frequency can be formulated in the form of [45]:

$$\sigma / \sigma_0 = F(f \varepsilon_0 \Delta\varepsilon / \sigma_0) \tag{16}$$

Room temperature scaling of AC conductivity with frequency has been observed according to Eq. (16) at different wt% of IL and depicted in Fig. 10(a). At different wt% of IL the curves merge as a single master curve showing similar kind of scaling dynamics. The effect of strong interaction of IL ions with that of MOF as well as with polymer segments can increase ion diffusion length by creating more free volume paths that enhance mobility of ions. The scaling of AC conductivity for 50 wt% of IL incorporated MOF-NiBTC-based PVdF-HFP nanocomposites at different temperatures are presented in Fig. 10 (b). At varying temperature the curves follow similar scaling behavior merging to a common ideal curve. The temperature independent scaling dynamics of charge carriers can be dealt with mismatch and relaxation model. This model depicts the idea of occurrence of heterogeneity or mismatch among newly migrating ions and already available ions in any particular coordinate site. Re-arrangement of ions can be done by frequent hopping of ions to the neighboring sites and that can be modulated by increasing temperature [46].

Analysis of electrochemical stability

The electrochemical stability of the MOF-NiBTC-based PVdF-HFP nanocomposites at different wt% of IL have been

Table 7 Frequency exponent *n* for room temperature variation of AC conductivity with angular frequency for MOF-NiBTC-based composite polymer electrolyte at different wt% of IL

Wt% of IL	Frequency exponent (n)
0%	0.67
30%	0.58
40%	0.49
50%	0.38

Table 8 Frequency exponent *n* for variation of AC conductivity with angular frequency for 50 wt% IL incorporated MOF-NiBTC-based composite polymer electrolyte at different temperatures

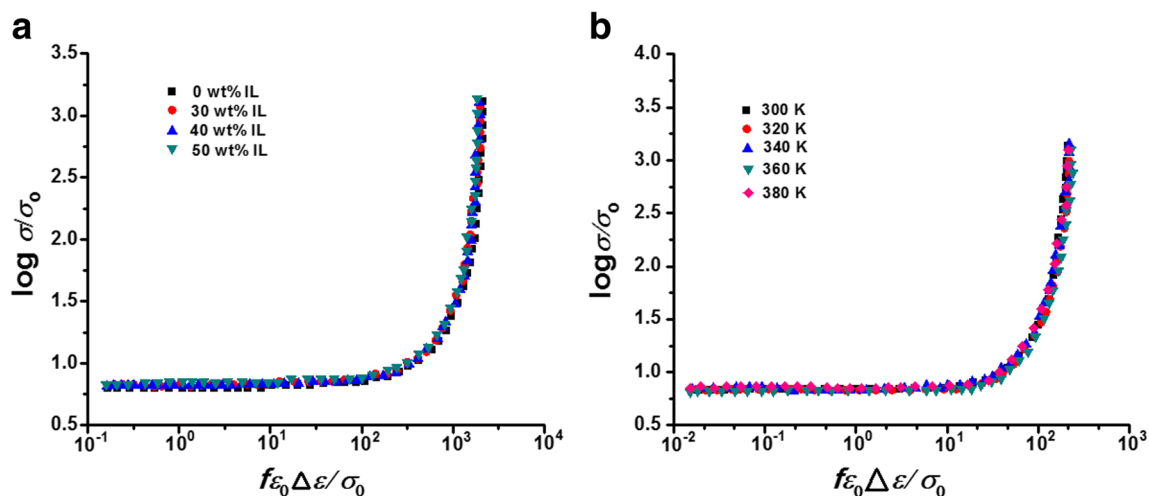| Temperature (K)	Frequency exponent (n)
300	0.38
320	0.34
340	0.31
360	0.28
380	0.25

Fig. 10 **a** Scaling of AC conductivity for MOF-NiBTC-based PVdF-HFP nanocomposites at different wt% of IL at room temperature (300 K). **b** Scaling of AC conductivity for MOF-NiBTC-based PVdF-HFP nanocomposites at 50 wt% of IL with varying temperature

studied by linear sweep voltammetry and shown in Fig. 11. In the electrochemical set up one Ag/AgCl electrode is used as reference electrode and two platinum electrodes are used as counter and working ones. No apparent current has been observed through working platinum electrode upto 3.8 V for the pristine nanocomposite having 0 wt% of IL. With increasing wt% of IL electrochemical stability increases and for the nanocomposite at 50 wt% of IL maximum stability is observed up to 5.7 V. The anionic contact with the electrode at the electrode-electrolyte interface may reduce electrochemical anodic stability due to irreversible oxidation of anions [47]. Strong interaction of BF_4^- ions with the Ni metal cluster of MOF can prevent the anionic motion through the polymer electrolyte to reduce the oxidation reaction at anode electrolyte interface that in turn increases electrochemical stability.
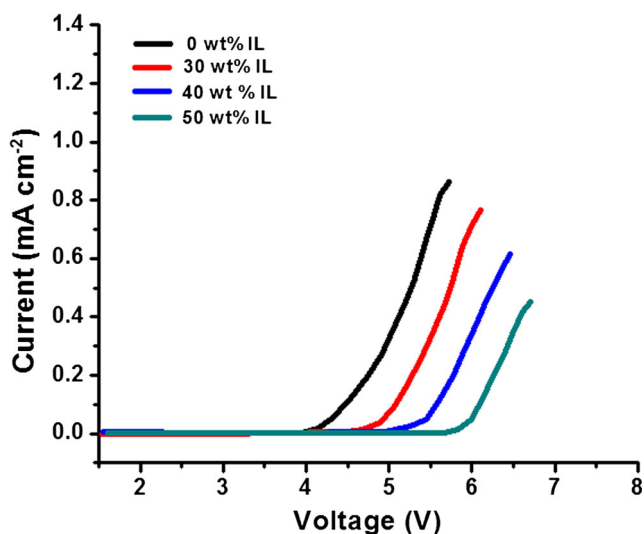
Conclusion

The structural and electrochemical properties of MOF-NiBTC-based PVdF-HFP nanocomposites have been studied at varying wt% of IL. From XRD results, reduction in degree of crystallinity has been observed as amorphicity of the nanocomposites increases with higher uptake of ionic liquid to enhance the mobility of polymer segments. Shifting of symmetric and asymmetric carboxylate modes is observed from FTIR spectra due to elongation of chemical bonds between Ni metal cluster and carboxyl groups with IL incorporation. From the analysis of XANES and EXAFS results, asymmetry in oscillatory behavior with reduction in coordination number is observed in Ni K-edge because of nanosizing effect of IL and strong interaction of BF_4^- anions with Ni metal cluster. HRTEM micrographs reveal compact and uniform structure of MOF nanoparticles upon IL incorporation. Appearance of agglomerated particles is seen, which is also confirmed by the BET results. The permittivity and modulus spectra depict non-Debye relaxation dynamics with low value of β_{KWW} with increasing wt% of IL. From the AC conductivity profile, lower value of frequency exponent n is observed with increasing IL concentration suggesting short range forward hopping of ions. The scaling dynamics of AC conductivity shows ion concentration and temperature independent behavior of the composite polymer electrolyte. Wide electrochemical stability up to 5.7 V and optimum ionic conductivity of 6.5×10^{-3} S cm^{-1} at 380 K has been obtained at 50 wt% of IL incorporation in the MOF-NiBTC-based composite polymer electrolyte system.

Fig. 11 Electrochemical stability analysis of MOF-NiBTC-based PVdF-HFP nanocomposites at different wt% of IL

References

1. Li J, Kupplerand RJ, Zhou H (2009) Chem Soc Rev 38(5):1477–1504
2. Shekhah O, Liu J, Fischer R, Woll C (2011) Chem Soc Rev 40(2):1081–1106
3. Bohrmanand JA, Carreon MA (2012) Chem Commun 48(42):5130–5132
4. Welton T (1997) Chem Rev 99(8):2071–2084
5. Seddon KR (1997) Chem Technol Biotechnol 68(4):351–356
6. Chen Y, Hu Z, Gupta Krishna M, Jianwen J (2011) J Phys Chem C 115(44):21736–21742
7. Kazuyuki F, Kazuya O, Ryuichi I, Teppei Y, Hiroshi K (2015) Chem Sci 6:4306–4310
8. Prestipino C, Regli L, Vitillo JG, Bonino F, Damin A, Lamberti C, Zecchina A, Solari PL, Kongshaug KO, Bordiga S (2006) Chem Mater 18(5):1337–1346
9. Sang X, Zhang J, Xiang J, Cui J, Zheng L, Zhang J, Wu Z, Li Z, Mo G, Xu Y, Song J, Liu C, Tan X, Luo T, Zhang B, Han B (2017) Nat Commun 8:1–7
10. Sciortino L, Alessi A, Messina F, Buscarino G, Gelardi FM (2015) J Phys Chem C 119:7826−7830
11. Morel FL, Pin S, Huthwelker T, Ranocchiari M, van Bokhoven JA (2015) Phys Chem Chem Phys 17(5):3326–3331
12. Muller M, Hermes S, Kahler K, van den Berg MWE, Muhler M, Fischer RA (2008) Chem Mater 20(14):4576–4587
13. Wright PV (1975) British Polym J 7(5):319–327
14. Polu AR, Rhee HW (2017) Int J Hydrog Energy 42(10):7212–7219
15. Pitawala J, Navarra MA, Scrosati B, Jacobsson P, Matic A (2014) J Power Sources 245:830–835
16. Hofmann A, Schulz M, Hanemann T (2013) Electrochim Acta 89:823–831
17. Weston JE, Steele BCH (1982) Solid State Ionics 7(1):75–79
18. Croce F, Appetecchi GB, Persi L, Scrosati B (1998) Nature 394(6692):456–458
19. Wieczorek W, Florjanczyk Z, Stevens JR (1995) Electrochim Acta 40:2251–2258
20. Gerbaldi C, Nair Jijeesh R, Kulandainathan Anbu M, Kumar Senthil R, Chiara F, Piercarlo M, Manuel SA (2014) J Mater Chem A 2:9948–9954
21. Farrukh I, Daye C, Yeongmin K, Kyung KD (2016) Ultrason Sonochem 31:93–101
22. Yuzhen H, Qi P, Junwen Z, Xiao F, Li S, Xiaotao F, Jingshu Z, Danni Y, Bo W (2015) ACS Appl Mater Interfaces 7:26608–26613
23. Saha D, Deng S (2009) Int J Hydrog Energy 34(6):2670–2678
24. Osada I, de Vries H, Scrosati B, Passerin S (2016) Angew Chem Int Ed 55:500–513
25. Dhumal Nilesh R, Singh Manish P, Anderson JA, Kiefer J, Kim JH (2016) J Phys Chem C 120:3295–3304
26. D'Souza L, Prabha D, Divya Shridhar MP, Naik Chandrakant G (2008) Anal Chem Insights 3:135–143
27. Sim LN, Majid SR, Arof AK (2012) Vib Spectrosc 58:57–66
28. Kumar TM, Shrikant P, Harish S, Khemraj B, Snehasis J (2015) Pharm Anal Acta 6:1000395
29. Srivastav A, Saxena Subha R, Sunil M, Singh Y (2012) Orient J Chem 28(3):1517–1529
30. Govind PS, De A, De U (2011) International Journal of Spectroscopy 2011:1–7
31. Singh R, Arora V, Tandon RP, Mansingh A, Chandra S (1999) Synth Met 104(2):137–144
32. Havriliak S, Negami S (1967) Polymer 8:161–210
33. Subhojtoti S, Kumar CS, Jiten G, Kumar MA (2014) J Phys D Appl Phys 47(27):275301–275313
34. Xi Y, Bin Y, Chiang CK, Matsuo M (2007) Carbon 45(6):1302–1309
35. Kohlrausch R (1847) Prog Anal Phys 123:393–399
36. Hazarika J, Kumar A (2014) Synth Met 198:239–247
37. Nath AK, Kumar A (2013) Solid State Ionics 253:8–17
38. Yang H, Zhuang GV, Ross PN (2006) J Power Sources 161(1):573–579
39. Asheesh K, Raghunandan S, Suresh M, Das Malay K, Kar Kamal K (2017) Journal of Elastomers & Plastics 49(6):513–526
40. Aziz Shujahadeen B, Woo Thompson J, Kadir MFZ, Ahmed Hameed M (2018) Journal of Science: Advanced Materials and Devices 3:1–17
41. Agrawal RC, Chandra A, Bhatt A, Mahipal YK (2008) New J Phys 10:043023–043033
42. Roling B, Martiny C, Funke K (1999) J Non-Cryst Solids 249(2-3):201–209
43. Jonscher AK (1977) Nature 267(5613):673–679
44. Mariappan CR, Govindaraj G (2002) Mater Sci Eng B 94(1):82–88
45. Papathanassiou AN, Sakellis I, Grammatikakis J (2010) Appl Phys Lett 97(4):041913
46. Funke K, Banhatti RD, Bruckner S, Cramer C, Krieger C, Mandanici A, Martiny C, Ross I (2002) Phys Chem Chem Phys 4(14):3155–3167
47. Park CH, Kim DW, Prakash J, Sun YK (2003) Solid State Ionics 159:111–119